

# A universal training scheme and the resulting universality for machine learning phases

Y.-H. Yseng<sup>1</sup>, F.-J. Jiang<sup>2\*</sup> and C.-Y. Huang<sup>3†</sup>

**1** Department of Physics, National Taiwan Normal University, 88, Sec.4, Ting-Chou Rd., Taipei 116, Taiwan

**2** Department of Physics, National Taiwan Normal University, 88, Sec.4, Ting-Chou Rd., Taipei 116, Taiwan

**3** Department of Applied Physics, Tunghai University, No. 1727, Sec. 4, Taiwan Boulevard, Xitun District, Taichung 40704, Taiwan

\* fjiang@ntnu.edu.tw † cyhuang@thu.edu.tw

May 19, 2022

## Abstract

An autoencoder (AE) and a generative adversarial networks (GANs) are trained only once on a one-dimensional (1D) lattice of 200 sites. Moreover, the AE contains only one hidden layer consisting of two neurons and both the generator and the discriminator of the GANs are made up of two neurons as well. The training set employed to train both the considered unsupervised neural networks (NN) is composed of two artificial configurations. Remarkably, despite their simple architectures, both the built AE and GANs have precisely determined the critical points of several models, including the three-dimensional (3D) classical  $O(3)$  model, the two-dimensional (2D) generalized classical XY model, the 2D two-state Potts model, and the 1D Bose-Hubbard model. The results presented here as well as that shown in *Eur. Phys. J. Plus* **136**, 1116 (2021) suggest that when phase transitions are considered, an elegant universal neural network that is extremely efficient and is applicable to broad physical systems can be constructed with ease. In particular, since a NN trained with two configurations can be applied to many models, it is likely that when machine learning is concerned, the majority of phase transitions belong to a class having two elements, i.e. the Ising class.

---

## Contents

<b>1</b>	<b>Introduction</b>	<b>2</b>
<b>2</b>	<b>The considered models</b>	<b>4</b>
<b>3</b>	<b>The constructed unsupervised NNs</b>	<b>5</b>
	3.1 Autoencoder	5
	3.2 Generative adversarial networks	5
<b>4</b>	<b>The benchmark calculations</b>	<b>6</b>

<b>5</b>	<b>The numerical results</b>	<b>7</b>
5.1	Constructing the required configurations for predictions	7
5.2	3D classical $O(3)$ model	8
5.2.1	AE results	8
5.2.2	GANs results	8
5.3	2D generalized $XY$ model	8
5.3.1	AE results	8
5.3.2	GANs results	9
5.4	2D two-state Potts model	9
5.4.1	AE results	9
5.4.2	GANs results	9
5.5	1D Bose-Hubbard model	11
5.5.1	AE results	12
5.5.2	GANs results	12
<b>6</b>	<b>Discussions and conclusions</b>	<b>12</b>
	<b>References</b>	<b>14</b>

---

## 1 Introduction

Machine learning (ML) techniques have gained dramatic attention recently in various fields of physics. Such examples include astronomy, particle physics, computational materials, and condensed matter physics [1–46]. While these applications are still in the exploratory stage, great improvement over the traditional approaches may be expected in the near future. Among the commonly used ML methods, neural networks (NNs), both supervised and unsupervised ones, are adopted in distinguishing various states of matters. They are considered in reproducing certain classical statistical distributions as well. Due to the many successful achievements of utilizing ML and NNs methods for physical problems, it is anticipated optimistically that promising breakthroughs in certain research fields of physics may be right around the corner.

One of the applications of NNs in physical problems is to detect different phases of matters. Indeed, for many systems and models, both supervised and unsupervised NNs have explored the associated phase diagrams with success to certain extents. Between the supervised and the unsupervised NNs, unsupervised ones are typically favored. This is because prior information is needed before one can apply the techniques of supervised NNs. As a result, the majority of NN studies for physical systems typically use unsupervised approaches.

While unsupervised NNs have dominated the applications of NNs in physical problems, supervised NNs have certain advantage over the unsupervised ones. For instance, supervised NNs are easier to implemented and often lead to better outcomes. Based on these facts, it is benefited to continue examining the potential applications of supervised NNs in reality.

Typically, applying a NN to study the properties of many-body systems has three stages, namely the training, the validation, and the testing (prediction) stages. Among these three stages, the training is the most time consuming one. In particular, with the conventional training strategy

usually employed in the literature, a new training is required whenever a new model or a different system size is considered. It should be pointed out that the configurations employed for the training are based on physical quantities such as the spins or the correlation functions. As a result, certain amount of computing time is needed to generate the relevant physical data in order to construct the required configurations for the NN training. These mentioned technical difficulties usually prevent the NNs from being used in real problems practically.

We would like to emphasize the fact that in the literature the NNs used to explore physical problems usually have very complicated architectures such as the deep learning convolutional neural networks (CNN). Such a strategy of building the NNs would lead to a lot of trainable (tunable) NN parameters. As a result, huge amount of computing time is required in order to obtain a working NN that has a dedicated architecture.

In Ref. [29], the two-dimensional (2D)  $q$ -state ferromagnetic Potts models on the square lattice are studied. Unlike the conventional training procedure which uses real Potts configurations generated by some numerical methods as the training set, the theoretical ground state configurations are employed instead. With this training strategy which costs much less computing time, accurate determinations of the critical points are obtained. Later in Refs. [45], two artificially made configurations on a one-dimensional (1D) lattice of 120 sites are used as the training sets, and the resulting (only one) supervised NN (which contains one hidden layer) has successfully determined the critical points of the three-dimensional (3D) classical  $O(3)$  model, the 2D classical  $XY$  (generalized classical  $XY$  model), a 3D dimerized spin-1/2 Heisenberg model, and the 3D 5-state ferromagnetic Potts model [45, 46]. It is remarkable that the (only one) simple supervised NN constructed in Ref. [45] is capable of studying the phase transitions of various 3D and 2D models. In particular, prior information is not necessary to carry out the investigations presented in Refs. [45, 46].

Although the fact that no information of the considered system is needed to utilize the supervised NN built in Ref. [45] makes the necessity of using unsupervised NNs no longer warranted, it is still interesting to examine whether the simple and elegant training approach in Ref. [45] can be adopted to train unsupervised NNs. Because of this motivation, here we train an autoencoder (AE) and a generative adversarial network (GAN) using two artificially made configurations on a 1D lattice of 200 sites. In particular, besides the input and the output layers, the AE built here contains only one hidden layer consisting of 2 neurons. Moreover, each of the generator and discriminator of the constructed GANs has only 2 neurons as well.

Remarkably, despite their simple architectures, the AE and the GANs obtained here with the elegant training strategy successfully estimate the critical points of various models, including the 3D classical  $O(3)$  model, the 2D 2-state Potts model, the 2D classical generalized  $XY$  model, as well as the 1D Bose-Hubbard model. We would like to emphasize the fact that both of these two unsupervised NNs have only been trained once, and no new training is conducted whenever new models or different system sizes are considered. It is amazing that two NNs, each of which in principle has only two neurons and is trained on a 1D lattice, can be adopted to calculate the critical points of many 3D, 2D and 1D models with high precision. In particular, no information of these studied models are needed for these two built unsupervised NNs to detect the associated phase transitions. Some benchmark investigations are carried out as well to demonstrate the efficiency of the NN(s) constructed here.

We would like to point out that with minor modification for the testing sets, it is likely the NNs obtained here and in Refs. [45, 46] can be directly applied to study other models such as the Fermi-Hubbard model as well as the Su-Schrieffer-Heeger (SSH) model.

Finally, it is worthy to mention that the results shown here and in Ref. [46] indicate that a NN

trained with only two (artificial) configurations can be applied to many physical models that vary from each other significantly. This implies that when machine learning is concerned, it is likely that the majority of phase transitions belong to a class having two elements, i.e. the Ising class.

The rest of the paper is organized as follows. After the introduction, the studied models are brief described in Sec. II. In Sec. III the employed unsupervised AE and GANs, the training strategy, and the built configurations for NN predictions are outlined. Benchmark calculations are demonstrated in Sec. IV and the obtained NN outcomes are presented in Sec. V. Sec. VI contains our discussions and conclusions.

## 2 The considered models

The Hamiltonians of the models considered here have the following expressions

1. 3D classical  $O(3)$  model [47, 48]:

$$\beta H_{O(3)} = -\beta \sum_{\langle ij \rangle} \vec{s}_i \cdot \vec{s}_j, \quad (1)$$

where  $\beta$  is the inverse temperature and  $\langle ij \rangle$  stands for the nearest neighbor sites  $i$  and  $j$ . In addition,  $\vec{s}_i$  appearing above is a unit vector belonging to a 3D sphere  $S^3$  and is located at site  $i$ .

2. 2D classical generalized XY model [49, 50]:

$$H_{\text{GXY}} = \sum_{\langle ij \rangle} -\Delta \cos(\theta_i - \theta_j) - (1 - \Delta) \cos(q\theta_i - q\theta_j), \quad (2)$$

where the summation is over the nearest neighbors  $i$  and  $j$ ,  $q$  is some (positive) integer, and  $0 \leq \theta_i \leq 2\pi$ . We will consider the case of  $\Delta = 0.25$  and  $q = 3$  in this study.

3. 2D 2-state Potts model [51]:

$$\beta H_{\text{Potts}} = -\beta \sum_{\langle ij \rangle} \delta_{\sigma_i, \sigma_j}. \quad (3)$$

Here  $\delta$  refers to the Kronecker function and the Potts variable  $\sigma_i$  at each site  $i$  takes an integer value from  $\{1, 2\}$ .

4. 1D Bose-Hubbard model: Using the creation and annihilation operators  $\hat{a}_i^\dagger$  and  $\hat{a}_i$ , the Hamiltonian of the 1D Bose-Hubbard model is given by [52, 53]

$$H_{\text{BH}} = -t \sum_{i=1}^L (\hat{a}_i^\dagger \hat{a}_{i+1} + \hat{a}_{i+1}^\dagger \hat{a}_i) + \frac{U}{2} \sum_{i=1}^L \hat{n}_i (\hat{n}_i - 1) - \mu \sum_{i=1}^L \hat{n}_i, \quad (4)$$

where  $L$  is the number of sites,  $t$  is the tunneling strength,  $U > 0$  is the on-site repulsive interaction strength,  $\mu$  is the chemical potential, and finally  $\hat{n}_i = \hat{a}_i^\dagger \hat{a}_i$  is the particle number operator at site  $i$ .

### 3 The constructed unsupervised NNs

Typically, a NN has many tunable parameters. In this investigation we use the default values for these parameters unless specified.

#### 3.1 Autoencoder

Using keras and tensorflow [54], the autoencoder employed here consists of one input layer, one hidden layer having two neurons, and one output layer. In particular, the hidden and the output layers are activated by the ReLU and the sigmoid functions, respectively. The definitions of these two activation functions are as follows

$$\text{ReLU}(x) = \max(0, x), \quad (5)$$

$$\text{sigmoid}(x) = \frac{1}{1 + e^x}. \quad (6)$$

The algorithm used for the training is minibatch, and one-hot encoding as well as  $L_2$  regularizations are also applied. We use 1000 epochs and the batch size is set to 30. Finally, the used loss function and optimizer are the crossentropy  $C$  and the adam, respectively. Here the definition of crossentropy  $C$  is given by

$$C = -\frac{1}{n} \sum_x y_x \ln b_x + (1 - y_x) \ln(1 - b_x), \quad (7)$$

where  $n$  is the total number of objects in the training set,  $b$  are the outcomes obtained after applying all the constructed layers. In addition,  $x$  and  $y$  are training inputs and the corresponding designed outputs, respectively. Figure 1 is a cartoon representation of the built AE.

For the training of the constructed AE, 200 copies of two artificially made configurations on a 1D lattice of 200 sites are used as the training set. Specifically, every site of 200 1D configurations takes the value of 1, and each of the other 200 configurations has 0 as the values for all of its elements. As we will demonstrate shortly, such a simple training set up can lead to a valid NN for learning various phases of all the considered models. For the reader who are interested in these machine learning terminologies associated with AE (and GANs which will be introduced later) are referred to Refs. [57, 58].

The magnitude  $R$  of the outputs is employed as the quantity for studying the targeted phase transitions. One expects that when  $R$  are considered as functions of temperature  $T$  (or  $\beta$ ), the associated outcomes will reveal the information relevant to  $T_c$  (or  $\beta_c$ ). Indeed, for the configurations obtained at low temperatures, they are of high similarity to the training sets. As a result, the associated outputs  $R$  have large magnitude. As the temperature  $T$  rises, the magnitude  $R$  of the outputs will decrease sharply at the critical point(s). As we will show later, this phenomenon is exactly what we have observed.

#### 3.2 Generative adversarial networks

The generative adversarial networks (GANs) considered here consists of a generator with 2 neurons and a discriminator with 2 neurons as well. Each of the 640 configurations for the generator consists of 200 sites and every site has -1 as its element. In addition, the training set is made up of 640 indential copies of 200 sites with all the elements being 1. Adam and crossentropy are the optimizer and the loss function employed, respectively. 2000 epochs is carried out and we use

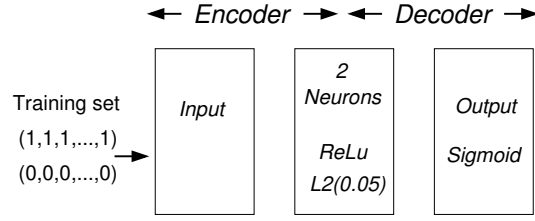


Figure 1: The AE employed in this study. The used AE consists of one input layer, one hidden layer of two neurons, and one output layer. The considered activation functions (and regularizer) are shown inside the boxes.

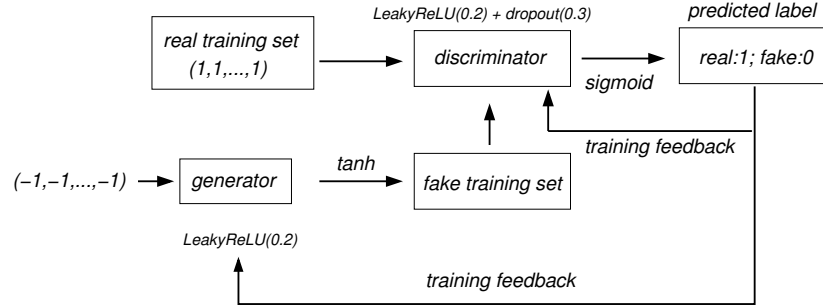


Figure 2: The GANs employed in this study.

128 as the batch size. The activation functions used are LeakyReLU, tanh, and sigmoid [57, 58]. The new activation functions LeakyReLU and tanh are defined as

$$\text{LeakyReLU}(x) = \begin{cases} \alpha x & \text{if } x < 0 \\ x & \text{if } x \geq 0 \end{cases} \quad (8)$$

$$\tanh(x) = \frac{e^x - e^{-x}}{e^x + e^{-x}}, \quad (9)$$

where  $\alpha$  is some constant. Finally, the algorithm used for the training is again minibatch and we also apply dropout at the discriminator. The predicted label is either 1 (true) or 0 (fake). Figure 2 is a cartoon representation of the GANs considered in this study.

Due to the data used for the fake and real training sets as well as the employed predicted label(s), the standard deviations (STD) of the outputs will be employed to explore the targeted phase transitions. One expects that the behavior of STD with respect to  $T$  (or  $\beta$ ) will disclose the information relevant to  $T_c$  (or  $\beta_c$ ). In particular, for configurations obtained at low temperatures, the related GANs outputs are either 1 or 0 with almost equal probabilities. Hence the associated outputs have large STD. As temperature  $T$  rises. The magnitude of STD will diminish dramatically at  $T_c$ .

## 4 The benchmark calculations

To demonstrate the efficiency of the AE constructed here, we have carried out certain benchmark calculations. In particular, the deep learning autoencoder (DLAE) built in Ref. [36] is employed here for the benchmark calculations (see figure 3). The model considered is the two-state ferromagnetic Potts model on the square lattice. In addition, the epochs and batch size used are

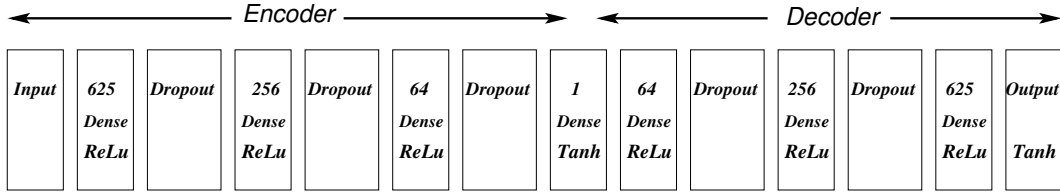


Figure 3: The deep learning AE employed in Ref. [36]. The considered activation functions and the number of neurons used are shown inside the boxes.

2000 and 30, respectively. Finally, the benchmark calculations are conducted on a server with two opetron 6344 and 96G memory.

The time required to train the AE with one hidden layer having two neurons is about 110 seconds, while the training using 30200 real (and full) Potts configurations obtained on 128 by 128 lattices as the training set for the DLAE shown in figure 3 takes about 302114 seconds to finish (It is anticipated that it will take longer to conduct all the DLAE trainings if various system sizes are considered). Here the number of configurations used for the conventional training is about the same as that used in Ref. [36]. Of course, the exact numbers of the benchmark calculations may depend on some factors such as whether CPU or GUP is considered for the execution of the calculations. Still, the results provide certain useful information regarding the performance of both the deep learning AE of Ref. [36] and the shallow AE used in this study. In any case, based on the benchmark outcomes, it is beyond doubt that the unconventional training strategy adopted here is more efficient than that typically used in the literature. Indeed, as we will demonstrate shortly, the precision of the determined critical points using the unsupervised NN built here is impressive as well.

## 5 The numerical results

To examine the validity as well as the efficiency of the constructed AE and GANs, certain configurations of the considered models are required. For the classical spin models these needed configurations are generated using Monte Carlo simulations with the Wolf cluster algorithm [55]. For the 1D Bose-Hubbard model, the worm algorithm of ALPS is considered [56].

### 5.1 Constructing the required configurations for predictions

Since the configurations used for the NN predictions should have the same dimensionality as those of the training sets, the needed configurations for the NN predictions using the AE and GANs constructed here should consist of 1D lattices of 200 sites.

For the  $O(3)$  model, the configurations built for the predictions are based on the spin variable  $\phi$ . Specifically, for a given  $O(3)$  spin configuration obtained from the Monte Carlo simulations, 200 spins are chosen randomly and uniformly. In addition, the  $\phi \bmod \pi$  of these 200 picked spins are used to construct the 1D configuration for the NN predictions associated with AE.

The same procedure is applied for the 2D generalized  $XY$  model. In particular, the  $\theta \bmod \pi$  of 200 spins, which are randomly picked from an original full spin configurations, are used as the elements of a 1D configuration for the predictions related to AE.

For every produced full Potts configuration of the two-state Potts model, 200 Potts variables  $\sigma$  are chosen randomly and the associated results of  $\sigma - 1$  are employed to build the 1D configuration

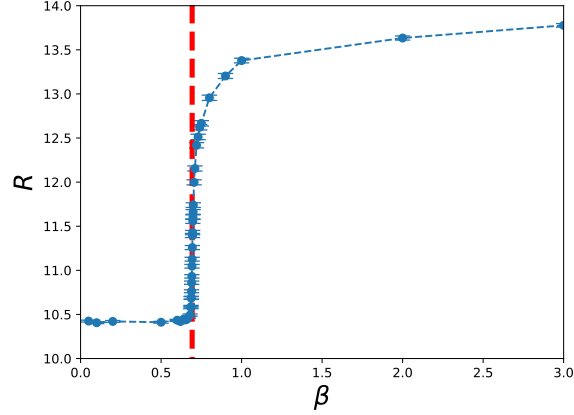


Figure 4: The magnitude  $R$  of the AE outputs as a function of the inverse temperature  $\beta$  for the 3D classical  $O(3)$  model. The system size is  $L=48$  and the vertical dashed line is the expected  $\beta_c$ . The value of  $R$  begins to rise significantly at  $\beta_c$ .

needed for the AE predictions.

Finally, for the 1D Bose-Hubbard model, the configurations used for the NN predictions are based on the local density.

Similar strategy is utilized to build the required configurations for the prediction related to GANs as well.

## 5.2 3D classical $O(3)$ model

### 5.2.1 AE results

The magnitude  $R$  of the AE outputs (In this study all the AE outputs are two hundred components vectors) as a function of the inverse temperature  $\beta$  for the 3D classical  $O(3)$  model is depicted in figure 4. The system size is  $L=48$  and the vertical dashed line in that figure is the expected critical inverse temperature  $\beta_c$ . The outcomes given in the figure imply that the value of  $R$  begins to rise significantly at  $\beta_c$ . In other words, how  $R$  behaves with respect to  $\beta$  reveals relevant information regarding the critical point. Particularly,  $\beta_c$  can be estimated to be the location in the associated parameter space that dramatical change of  $R$  takes place.

### 5.2.2 GANs results

The standard deviations (STD) of the GANs outputs (The GANs outputs are numbers between 0 and 1) as a function of  $\beta$  for the 3D classical  $O(3)$  model is shown in fig. 5. The linear system size  $L$  for the data in the figure is  $L = 48$ . As expected, the figure demonstrates that the value of STD rises dramatically at  $\beta_c$ . The shown outcomes indicate the STD of the NN outputs indeed can be employed to locate the critical point  $\beta_c$ .

## 5.3 2D generalized $XY$ model

### 5.3.1 AE results

The magnitude  $R$  of the AE outputs as a function of the temperature  $T$  for the 2D generalized classical  $XY$  model is shown in fig. 6. The system size is  $L = 128$ . The vertical dashed and solid lines



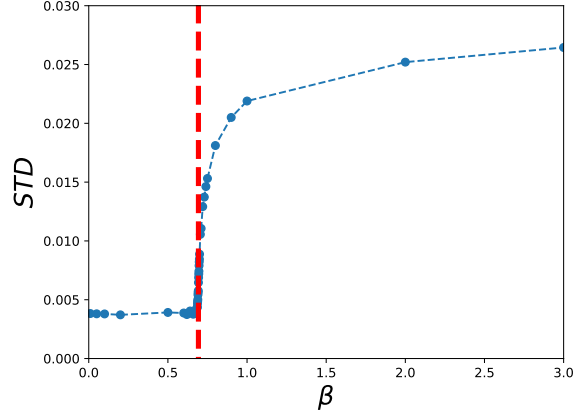


Figure 5: The standard deviations (STD) of the GANs outputs as a function of the inverse temperature  $\beta$  for the 3D classical  $O(3)$  model. The system size is  $L = 48$  and the vertical dashed line is the expected  $\beta_c$ . The value of STD begins to rise significantly at  $\beta_c$ .

in the figure are the expected  $T_{c,\text{Potts}}$  and  $T_{c,\text{BKT}}$  associated with the 3-state Potts and the Berezinskii–Kosterlitz–Thouless (BKT) universalities, respectively. As can be seen from the figure, a sudden jump of  $R$  occurs at  $T_{c,\text{Potts}}$ . Moreover, close  $T_{c,\text{BKT}}$  the behavior of  $R$  shows an apparent drop as well. These observed phenomena obviously indicate that the locations of critical points in the parameter space can be estimated by the  $T$ -dependence of  $R$ . It is also interesting to notice that the drop of  $R$  at  $T_{c,\text{BKT}}$  is less sharp than that at  $T_{c,\text{Potts}}$ . This observation is consistent with the fact that BKT transitions receive certain logarithmic corrections, hence only with extremely large system size will the signal of the transitions appear transparently.

### 5.3.2 GANs results

The standard deviations (STD) of the GANs outputs as a function of  $T$  for the 2D generalized classical  $XY$  model is shown in fig. 7. The linear system size  $L$  for the data in the figure is  $L = 128$ . As expected, the figure demonstrates that the value of STD diminishes dramatically at  $T_{c,\text{Potts}}$  and  $T_{c,\text{BKT}}$ . We would like to emphasize the fact that when the outcomes in fig. 7 are compared with that in fig. 5, the drop of STD at  $T_{c,\text{BKT}}$  is less abrupt. This indicates that when BKT transitions are concerned, AE has better performance of detecting their existence than that of GANs.

## 5.4 2D two-state Potts model

### 5.4.1 AE results

The magnitude  $R$  of the AE outputs as a function of the temperature  $T$  for the 2D two-state Potts model is shown in fig. 8. The system size is  $L = 120$  and the vertical dashed line is the expected  $T_c$ . Clearly the outcomes demonstrated in the figure imply that  $R$  drops significantly at  $T_c$ .

### 5.4.2 GANs results

The standard deviations (STD) of the GANs outputs as a function of  $T$  for the two-state Potts model is shown in fig. 9. The linear system size  $L$  for the data in the figure is  $L = 120$  and the

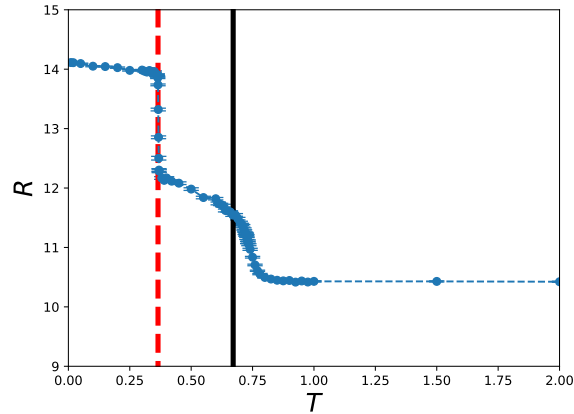


Figure 6: The magnitude  $R$  of the AE outputs as a function of the temperature  $T$  for the 2D generalized classical  $XY$  model. The system size is  $L = 128$ . The vertical dashed and solid lines are the expected  $T_c$  associated with the 3-state Potts and the Berezinskii–Kosterlitz–Thouless (BKT) universalities, respectively. The value of  $R$  drops obviously at  $T_{c,\text{Potts}}$  and  $T_{c,\text{BKT}}$ .

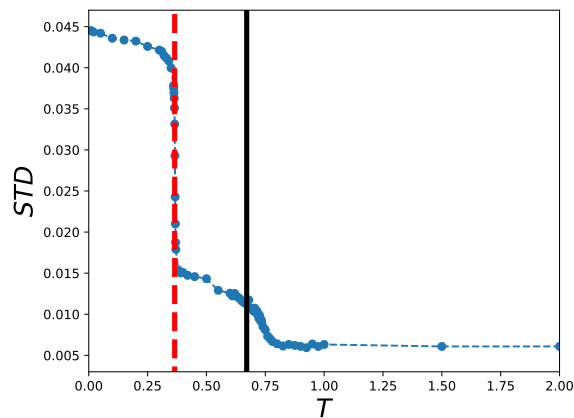


Figure 7: The standard deviations of the NN (GANs) outputs as a function of the temperature  $T$  for the 2D generalized classical  $XY$  model. The system size is  $L=128$ . The vertical dashed and solid lines are the expected  $T_c$  associated with the 3-state Potts and the BKT universalities, respectively. The value of STD drops obviously at  $T_{c,\text{Potts}}$  and  $T_{c,\text{BKT}}$ .

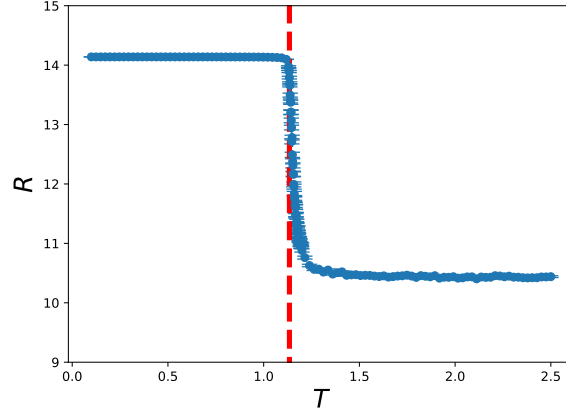


Figure 8: The magnitude  $R$  of the AE outputs as a function of the temperature  $T$  for the 2D two-state Potts model. The system size is  $L=120$ . The vertical dashed line is the expected  $T_c$ . The value of  $R$  drops dramatically at  $T_c$ .

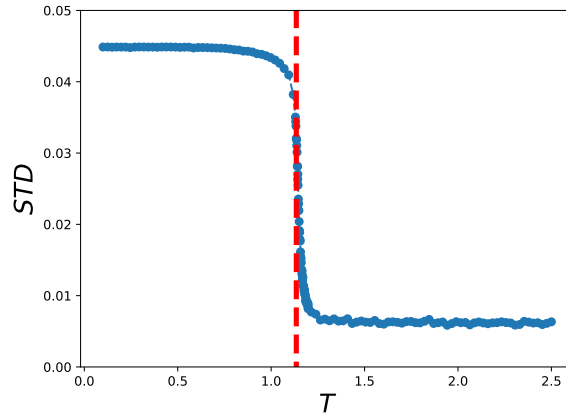


Figure 9: The standard deviations STD of the GANs outputs as a function of the temperature  $T$  for the 2D two-state Potts model. The system size is  $L = 120$  and the vertical dashed line is the expected  $T_c$ . The value of STD drops dramatically at  $T_c$ .

vertical dashed line is the expected  $T_c$ . As expected, the figure demonstrates that the value of STD drops dramatically at  $T_c$ .

## 5.5 1D Bose-Hubbard model

The associated simulations are conducted with system size  $L = 256$ ,  $t = 0.1$ ,  $U = 1.0$ ,  $T = 0.0025$ , and various values of  $\mu$ . As  $\mu$  varies, one expects to see a transition from the superfluidity to the Mott insulator. In addition, the maximum number of Bose per site is set to 5, and the naive configurations used for the NN prediction are built from the local densities which are generated based on the means and the mean errors of the outcomes from the Monte Carlo simulations. Finally, in the process of one-hot encoding, if the local density  $n_i$  of an original site  $i$  is greater (smaller) than 0.99 (i.e. we set a density cut off to be 0.01), then integer 1 (0) is assigned to the associated spot.

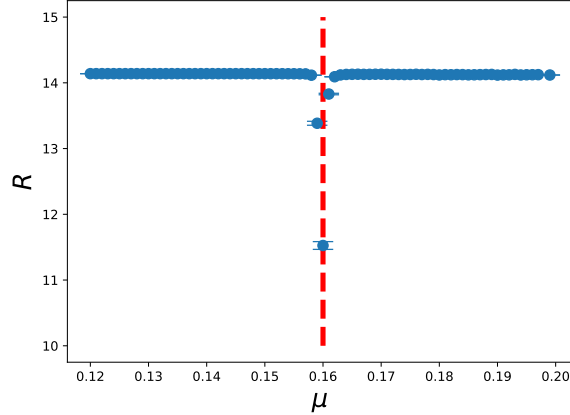


Figure 10: The magnitude  $R$  of the AE outputs as a function of  $\mu$  for the 1D Bose-Hubbard model. The vertical dashed line is the expected  $\mu_c$ .

### 5.5.1 AE results

The magnitude  $R$  of the AE outputs as a function of  $\mu$  is shown in fig. 10. The dashed vertical line in the figure is the critical point  $\mu_c$  estimated from Refs. [52, 53]. As can be seen from the figure, the  $\mu$  which has the smallest value of  $R$  is very close to  $\mu_c$ . In other words, the constructed AE is capable of detecting the considered phase transition of the 1D Bose-Hubbard model. Here we would like to point out that if one uses another value of density cut off, then the  $\mu$  having the minimum  $R$  clearly will shift (slightly). This will have certain impact on estimating  $\mu_c$ . It is obviously that such an impact will become much milder if extremely accurate data points (so that the density cut off can be very tiny) are used for the (NN) calculations.

### 5.5.2 GANs results

For the GANs, when the detection of the phase transition (of the 1D Bose-Hubbard model) is concerned, the performance of the outputs themselves is better than that of the standard deviation. Indeed, as can be seen from fig. 11, the  $R$  drops significantly when one approaches  $\mu_c$  (the vertical dashed line) from the left. Here again a density cut off of 0.01 is considered. It should be pointed out that unlike those used in the previous sections, the GANs leading to the results present in fig. 11 has been trained with the additional step of one-hot encoding.

## 6 Discussions and conclusions

In this study, an AE having only one hidden layer of two neurons as well as a GANs with 2 neurons generator and 2 neurons discriminator are constructed. In particular, they are trained only once on a 1D lattice of 200 sites. The training set used consists of two artificial configurations. The obtained unsupervised NNs successfully determine the critical points of several models, including the 3D classical  $O(3)$  model, the 2D generalized classical  $XY$  model, the 2D two-state Potts model, as well as the 1D Bose-Hubbard model. It is remarkable that an AE and a GANs with such simple architectures can lead to high precision calculations of the targeted phase transitions. It is beyond doubt that with moderate modifications, the applications of the built AE and GANs here can be

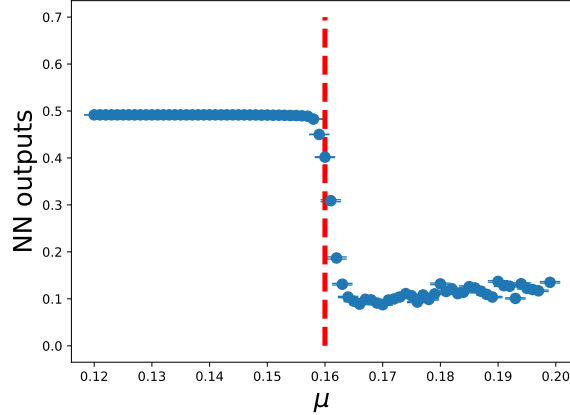


Figure 11: The GANs outputs as a function of  $\mu$  for the 1D Bose-Hubbard model. The vertical dashed line is the expected  $\mu_c$ .

extended to include the Fermi-Hubbard or SSH models. It is amazing as well that any of the two unsupervised NNs built here can be employed to calculate the critical points of various 3D and 2D models accurately. In particular, the constructed AE and GANs are able to successfully detect both the symmetry breaking and the topology related phase transitions. It is also surprising that no information of these models is needed for the built AE and GANs to detect the associated phase transitions.

When compared with the conventional deep learning AEs typically used in the literature, a benchmark investigation indicates that at least several thousand speed up is gained for the AE employed here. Certain gain in the calculations of prediction conducted here is anticipated as well. Finally, we would like to mention that the training of the GANs considered in this study is also extremely efficient. Specifically, it takes about 154 seconds to train the GANs (with 2000 epochs) [59].

It should be pointed out that in Ref. [25], a supervised NN with one hidden layer of two neurons has successfully determined the  $T_c$  of the 2D Ising model. Here we have gone much further than that achieved in Ref. [25].

For each of the models studied here, only one system size data is considered. Definitely one can carry out the needed calculations to obtain results of several box sizes. With these new outcomes, semi-experimental finite-size scaling ansatz can be utilized to reach an estimation of the bulk critical point(s) [42, 46]. Here we do not perform such an investigation since relevant detailed studies are available in Refs. [42, 46].

We would also like to emphasize the fact that the conventional training methods that usually used in the literature is computational demanding and require huge amount of computer memory. Hence, most of the calculations are limited to small to moderate large system sizes. Similar to the supervised NN considered in Refs. [42, 46], there is no system size restriction for the built AE and GANs employed here.

In addition to the advantage of extremely efficient training, with the method adopted here much less storage capacity is required when compared with the standard NN approaches used in the literature as well. Practically one only needs to save 200 spins for every generated large system size configuration which usually comes with several thousand to over 10 thousand spins. This feature is similar to the supervised NN employed in Ref. [42, 46]. To demonstrate the high efficiency of the employed unsupervised NNs, we have recorded the total time needed to complete

the NN calculations associated with the 3D  $O(3)$  model. The 3D  $O(3)$  model is chosen because it takes the longest time to perform the related NN investigation for this model using the conventional approaches. For the AE considered in this study, from the start of the training to the end of the prediction the time needed for these procedures is about 200 seconds (This also includes the time required for reading (loading) the data files). In other words, it takes less than 4 minutes to produce the results shown in fig. 4. Here for each of the 49 temperatures, two thousand configurations are used for the NN prediction. In reality, one can only keep two hundred relevant quantities (such as the spins) for every generated configurations and uses these data to perform the NN prediction with the AE and GANs constructed here. As a result, it is anticipated that if the same amount of data are employed, then the required time to complete the whole NN calculations for each of the other studied models is about the same as that of the 3D  $O(3)$  model.

Based on the results obtained here as well as that in Ref. [45], it is likely that the training schemes introduced here and in Ref. [45] are the most efficient strategy for training when studying phase transitions with NN are concerned. In addition, these outcomes show that a NN trained once with two artificial configurations can be applied to many models that are different from each other dramatically. This suggests strongly that when machine learning is considered, many, or even the majority of phase transitions belong to a class having two elements, namely the Ising class.

Finally, it will be interesting to examine whether by simply engineering the configurations for prediction one can apply the unsupervised NN constructed here to study the criticalities of some other models that are not investigated in this study. It is also interesting to see if similar elegant ideas exist for other research fields of physics.

## Acknowledgements

**Funding information** Partial support from the Ministry of Science and Technology of Taiwan (MOST) is acknowledged (MOST 110-2112-M-003-015 and MOST 108-2112-M-029-006-MY3).

## References

- [1] John C. Snyder, Matthias Rupp, Katja Hansen, Klaus-Robert Müller, and Kieron Burke, Phys. Rev. Lett. **108** 253002 (2012). doi:[10.1103/PhysRevLett.108.253002](https://doi.org/10.1103/PhysRevLett.108.253002)
- [2] Zhenwei Li, James R. Kermode, and Alessandro De Vita, Phys. Rev. Lett. **114**, 096405 (2015). doi:[10.1103/PhysRevLett.114.096405](https://doi.org/10.1103/PhysRevLett.114.096405)
- [3] P. Baldi, P. Sadowski and D. Whiteson, Phys. Rev. Lett. **114**, 111801 (2015). doi:[10.1103/PhysRevLett.114.111801](https://doi.org/10.1103/PhysRevLett.114.111801)
- [4] P Baldi, K. Bauer, C. Eng, P Sadowski and D. Whiteson, Phys. Rev. D **93**, 094034 (2016). doi:[10.1103/PhysRevD.93.094034](https://doi.org/10.1103/PhysRevD.93.094034)
- [5] B. Hoyle, Astron. Comput. **16**, 34-40 (2016). doi:[10.1016/j.ascom.2016.03.006](https://doi.org/10.1016/j.ascom.2016.03.006)
- [6] Giacomo Torlai and Roger G. Melko, Phys. Rev. B **94**, 165134 (2016). doi:[10.1103/PhysRevB.94.165134](https://doi.org/10.1103/PhysRevB.94.165134)
- [7] Lei Wang, Phys. Rev. B **94**, 195105 (2016). doi:[10.1103/PhysRevB.94.195105](https://doi.org/10.1103/PhysRevB.94.195105)

- [8] A. Mott, J. Job, J. R. Vlimant, D. Lidar and M. Spiropulu, *Nature* **550**, no.7676, 375-379 (2017). doi:[10.1038/nature24047](https://doi.org/10.1038/nature24047)
- [9] Peter Broecker, Juan Carrasquilla, Roger G. Melko, and Simon Trebst, *Scientific Reports* **7**, 8823 (2017). doi:[10.1038/s41598-017-09098-0](https://doi.org/10.1038/s41598-017-09098-0)
- [10] Juan Carrasquilla, Roger G. Melko, *Nature Physics* **13**, 431–434 (2017). doi:[10.1038/nphys4035](https://doi.org/10.1038/nphys4035)
- [11] J. Tubiana and R. Monasson, *Phys. Rev. Lett.* **118**, 138301 (2017). doi:[10.1103/PhysRevLett.118.138301](https://doi.org/10.1103/PhysRevLett.118.138301)
- [12] Kolb, B., Lentz, L. C. and Kolpak, A. M., *Sci Rep* **7**, 1192 (2017). doi:[10.1038/s41598-017-01251-z](https://doi.org/10.1038/s41598-017-01251-z)
- [13] Evert PL. van Nieuwenburg, Ye-Hua Liu, Sebastian D. Huber, *Nature Physics* **13**, 435–439 (2017). doi:[10.1038/nphys4037](https://doi.org/10.1038/nphys4037)
- [14] Giuseppe Carleo, Matthias Troyer, *Science* **355**, 602 (2017). doi:[10.1126/science.aag2302](https://doi.org/10.1126/science.aag2302)
- [15] Yuki Nagai, Huitao Shen, Yang Qi, Junwei Liu, and Liang Fu *Phys. Rev. B* **96** 161102 (2017). doi:[10.1103/PhysRevB.96.161102](https://doi.org/10.1103/PhysRevB.96.161102)
- [16] Dong-Ling Deng, Xiaopeng Li, and S. Das Sarma, *Phys. Rev. B* **96** 195145 (2017). doi:[10.1103/PhysRevB.96.195145](https://doi.org/10.1103/PhysRevB.96.195145)
- [17] Yi Zhang, Roger G. Melko, and Eun-Ah Kim *Phys. Rev. B* **96**, 245119 (2017). doi:[10.1103/PhysRevB.96.245119](https://doi.org/10.1103/PhysRevB.96.245119)
- [18] Wenjian Hu, Rajiv R. P. Singh, and Richard T. Scalettar, *Phys. Rev. E* **95**, 062122 (2017). doi:[10.1103/PhysRevE.95.062122](https://doi.org/10.1103/PhysRevE.95.062122)
- [19] Yi Zhang and Eun-Ah Kim, *Phys. Rev. Lett.* **118**, 216401 (2017). doi:[10.1103/PhysRevLett.118.216401](https://doi.org/10.1103/PhysRevLett.118.216401)
- [20] Akinori Tanaka and Akio Tomiya, *J. Phys. Soc. Jpn.* **86**, 063001 (2017).
- [21] Matthew J. S. Beach, Anna Golubeva, and Roger G. Melko, *Phys. Rev. B* **97**, 045207 (2018). doi:[10.1103/PhysRevB.97.045207](https://doi.org/10.1103/PhysRevB.97.045207)
- [22] Kelvin Ch'ng, Nick Vazquez, and Ehsan Khatami, *Phys. Rev. E* **97**, 013306 (2018). doi:[10.1103/PhysRevE.97.013306](https://doi.org/10.1103/PhysRevE.97.013306)
- [23] L. G. Pang, K. Zhou, N. Su, H. Petersen, H. Stöcker and X. N. Wang, *Nature Commun.* **9**, no.1, 210 (2018). doi:[10.1038/s41467-017-02726-3](https://doi.org/10.1038/s41467-017-02726-3)
- [24] Lu, S., Zhou, Q., Ouyang, Y. et al., *Nat Commun* **9**, 3405 (2018). doi:[10.1038/s41467-018-05761-w](https://doi.org/10.1038/s41467-018-05761-w)
- [25] Dongkyu Kim, Dong-Hee Kim, *Phys. Rev. E* **98**, 022138 (2018). doi:[10.1103/PhysRevE.98.022138](https://doi.org/10.1103/PhysRevE.98.022138)
- [26] Keith T. Butler, Daniel W. Davies, Hugh Cartwright, Olexandr Isayev, and Aron Walsh, *Nature* **559**, 547–555 (2018). doi:[10.1038/s41586-018-0337-2](https://doi.org/10.1038/s41586-018-0337-2)

- [27] Albert P. Bartók, James Kermode, Noam Bernstein, and Gábor Csányi, Phys. Rev. X **8**, 041048 (2018). doi:[10.1103/PhysRevX.8.041048](https://doi.org/10.1103/PhysRevX.8.041048)
- [28] Phiala E. Shanahan, Daniel Trewartha, and William Detmold, Phys. Rev. D **97**, 094506 (2018). doi:[10.1103/PhysRevD.97.094506](https://doi.org/10.1103/PhysRevD.97.094506)
- [29] C.-D. Li, D.-R. Tan, and F.-J. Jiang, Annals of Physics, 391 (2018) 312-331. doi:[10.1016/j.aop.2018.02.018](https://doi.org/10.1016/j.aop.2018.02.018)
- [30] Pankaj Mehta, Marin Bukov, Ching-Hao Wang, Alexandre G.R. Day, Clint Richardson, Charles K. Fisher, and David J. Schwab, Phys. Rep. **810**, (2019) 1-124. doi:[10.1016/j.physrep.2019.03.001](https://doi.org/10.1016/j.physrep.2019.03.001)
- [31] Giuseppe Carleo, Ignacio Cirac, Kyle Cranmer, Laurent Daudet, Maria Schuld, Naftali Tishby, Leslie Vogt-Maranto, and Lenka Zdeborová, Rev. Mod. Phys. **91**, 045002 (2019). doi:[10.1103/RevModPhys.91.045002](https://doi.org/10.1103/RevModPhys.91.045002)
- [32] Wanzhou Zhang, Jiayu Liu, and Tzu-Chieh Wei, Phys. Rev. E **99**, 032142 (2019). doi:[10.1103/PhysRevE.99.032142](https://doi.org/10.1103/PhysRevE.99.032142)
- [33] Jonas Greitemann, Ke Liu, and Lode Pollet, Phys. Rev. B **99**, 060404(R) (2019). doi:[10.1103/PhysRevB.99.060404](https://doi.org/10.1103/PhysRevB.99.060404)
- [34] Xiao-Yu Dong, Frank Pollmann, and Xue-Feng Zhang, Phys. Rev. B **99**, 121104(R) (2019). doi:[10.1103/PhysRevB.99.121104](https://doi.org/10.1103/PhysRevB.99.121104)
- [35] Kouji Kashiwa, Yuta Kikuchi, and Akio Tomiya, Prog. Theor. Exp. Phys., 2019, 083A04 (2019). doi:[10.1093/ptep/ptz082](https://doi.org/10.1093/ptep/ptz082)
- [36] Constantia Alexandrou, Andreas Athenodorou, Charalambos Chrysostomou, Srijit Paul, Eur. Phys. J. B (2020) 93: 226. doi:[10.1140/epjb/e2020-100506-5](https://doi.org/10.1140/epjb/e2020-100506-5)
- [37] A. J. Larkoski, I. Moulton and B. Nachman, Phys. Rept. **841**, 1-63 (2020). doi:[10.1016/j.physrep.2019.11.001](https://doi.org/10.1016/j.physrep.2019.11.001)
- [38] X. Han and S. A. Hartnoll, Phys. Rev. X **10**, 011069 (2020). doi:[10.1103/PhysRevX.10.011069](https://doi.org/10.1103/PhysRevX.10.011069)
- [39] D.-R. Tan *et al.* 2020 New J. Phys. **22** 063016. doi:[10.1088/1367-2630/ab8ab4](https://doi.org/10.1088/1367-2630/ab8ab4)
- [40] G. Aad *et al.* [ATLAS], Phys. Rev. Lett. **125**, no.13, 131801 (2020). doi:[10.1103/PhysRevLett.125.131801](https://doi.org/10.1103/PhysRevLett.125.131801)
- [41] R. Morgan *et al.* [DES], Astrophys. J. **901**, no.1, 83 (2020). doi:[10.3847/1538-4357/abafaa](https://doi.org/10.3847/1538-4357/abafaa)
- [42] D.-R. Tan and F.-J. Jiang, Phys. Rev. B **102**, 224434 (2020). doi:[10.1103/PhysRevB.102.224434](https://doi.org/10.1103/PhysRevB.102.224434)
- [43] A. Lidiak and Z. Gong, Phys. Rev. Lett. **125**, no.22, 225701 (2020). doi:[10.1103/PhysRevLett.125.225701](https://doi.org/10.1103/PhysRevLett.125.225701)
- [44] K. A. Nicoli, C. J. Anders, L. Funcke, T. Hartung, K. Jansen, P. Kessel, S. Nakajima and P. Stornati, Phys. Rev. Lett. **126**, no.3, 032001 (2021). doi:[10.1103/PhysRevLett.126.032001](https://doi.org/10.1103/PhysRevLett.126.032001)



- [45] D.-R. Tan, J.-H. Peng, Y.-H. Tseng and F.-J. Jiang, Eur. Phys. J. Plus (2021) **136**: 1116. doi:[10.1140/epjp/s13360-021-02121-4](https://doi.org/10.1140/epjp/s13360-021-02121-4)
- [46] Y.-H. Tseng and F.-J. Jiang, Results in Physics 33 (2022) 105134. doi:[10.1016/j.rinp.2021.105134](https://doi.org/10.1016/j.rinp.2021.105134)
- [47] Christian Holm and Wolfhard Janke, Phys. Lett. A **173** (1993) 8. doi:[10.1016/0375-9601\(93\)90077-D](https://doi.org/10.1016/0375-9601(93)90077-D)
- [48] Massimo Campostrini, Martin Hasenbusch, Andrea Pelissetto, Paolo Rossi, and Ettore Vicari, Phys. Rev. B **65**, 144520 (2002). doi:[10.1103/PhysRevB.65.144520](https://doi.org/10.1103/PhysRevB.65.144520)
- [49] Gabriel A. Canova, Yan Levin, and Hefferson J. Arenzon, Phys. Rev. E **89**, 012126 (2014). doi:[10.1103/PhysRevE.89.012126](https://doi.org/10.1103/PhysRevE.89.012126)
- [50] Gabriel A. Canova, Yan Levin, and Hefferson J. Arenzon, Phys. Rev. E **94**, 032140 (2016). doi:[10.1103/PhysRevE.94.032140](https://doi.org/10.1103/PhysRevE.94.032140)
- [51] F. Y. Wu, Rev. Mod. Phys. **54**, 235 (1982). doi:[10.1103/RevModPhys.54.235](https://doi.org/10.1103/RevModPhys.54.235)
- [52] S. Ejima, H. Fehske, and F. Gebhard, EPL, 93 (2011) 30002. doi:[10.1209/0295-5075/93/30002](https://doi.org/10.1209/0295-5075/93/30002)
- [53] Satoshi Ejima, Holger Fehske, Florian Gebhard, Kevin zu Münster, Michael Knap, Enrico Arrigoni, and Wolfgang von der Linden, Phys. Rev. A **85**, 053644 (2012). doi:[10.1103/PhysRevA.85.053644](https://doi.org/10.1103/PhysRevA.85.053644)
- [54] <https://keras.io>; <https://www.tensorflow.org>.
- [55] U. Wolff, Phys. Rev. Lett. **62**, 361 (1989). doi:[10.1103/PhysRevLett.62.361](https://doi.org/10.1103/PhysRevLett.62.361)
- [56] B Bauer et al, J. Stat. Mech. (2011) P05001. doi:[10.1088/1742-5468/2011/05/P05001](https://doi.org/10.1088/1742-5468/2011/05/P05001).
- [57] Sebastian Raschka and Vahid Mirjalili, *Python Machine Learning: Machine Learning and Deep Learning with Python, scikit-learn, and TensorFlow 2*, 3rd edition, Packt, Birmingham, UK (2019).
- [58] Aurélien Géron, *Hands-On Machine Learning with Scikit-Learn, Keras, and TensorFlow: Concepts, Tools, and Techniques to Build Intelligent Systems*, 2nd edition, O'Reilly Media, Sebastopol, CA (2019).
- [59] It takes about 388 seconds to train the GANs with the step of one-hot encoding.